RESEARCH ARTICLE

NANO · MICRO small
www.small-journal.com

NIR-Induced Photoswitching Hybrid DNA Nanoconstruct-Based Drug Delivery System for Spatiotemporal Control of Stem Cell Fate

Thanapat Pongkulapa, Ji Hye Yum, Callan D. McLoughlin, Brandon Conklin, Tomotaka Kumagai, Li Ling Goldston, Hiroshi Sugiyama, Soyoung Park, and Ki-Bum Lee**

Precise spatiotemporal control of drug delivery is extremely valuable for regulating stem cell fate, particularly in stem cell differentiation. A novel near-infrared (NIR)-mediated spatiotemporal delivery system is reported combining photo-switchable arylazopyrazole (AAP)-containing DNA strands and upconversion nanoparticles (UCNPs). This nano-drug delivery system (NDDS) enables precise modulation of DNA duplex structures in response to NIR stimuli, overcoming the limitations of traditional UV-responsive systems. AAP derivatives with enhanced photoswitching efficiency (≈98%) and significantly improved cis-form stability are engineered. The successful delivery of curcumin, a neurogenic compound with an affinity for the minor groove of DNA, to human neural stem cells (NSCs) is achieved using UCNP-DNA-AAP constructs. Upon 980 nm NIR light exposure, UCNPs efficiently up-converted NIR to UV light, triggering AAP photoisomerization and DNA dissociation, thus releasing curcumin. This approach enabled efficient spatiotemporal control over NSC differentiation while facilitating neuroprotection. Immunofluorescence and gene expression analyses demonstrated enhanced neuronal mRNA levels and neurite outgrowth in treated cells. In short, the NIR-mediated photo-switchable NDDS offers a precise and innovative approach to control stem cell fate, enabling spatiotemporal regulation of cellular processes. This technology has significant potential applications in nanomedicine and neuroscience, where precise drug delivery is crucial for targeted neural interventions.

1. Introduction

Achieving precise control over the release of drugs, in both spatial and temporal dimensions, is extremely valuable for guiding the differentiation and behavior of stem cells. This intricate process requires the coordinated delivery of biochemical signals and physical stimuli, which must be precisely orchestrated. By ensuring timely and localized control, critical stem cell processes, such as proliferation, migration, and differentiation, can be effectively regulated and directed toward desired therapeutic outcomes.[1–3] In recent years, innovative methods have emerged to effectively regulate biomolecular complexes using external stimuli, such as temperature, magnetic fields, and light-responsive regulation. These approaches offer a means to control dynamic and complex biological processes.[4,5] Light is particularly notable among these stimuli for its ability to control biological functions with high temporal and spatial precision. Specifically, NIR light is an excellent candidate for investigating and manipulating the spatiotemporal dynamics of signals within living neural cells and

T. Pongkulapa, C. D. McLoughlin, B. Conklin, L. L. Goldston, K.-B. Lee
Department of Chemistry and Chemical Biology
Rutgers, The State University of New Jersey
Piscataway, NJ 08854, USA
E-mail: kblee@rutgers.edu

The ORCID identification number(s) for the author(s) of this article can be found under https://doi.org/10.1002/smll.202409530

DOI: 10.1002/smll.202409530

J. H. Yum, T. Kumagai, H. Sugiyama, S. Park
Department of Chemistry
Graduate School of Science
Kyoto University
Kitashirakawa-oiwakecho, Sakyo-ku, Kyoto 606–8502, Japan
E-mail: spark@ifrec.osaka-u.ac.jp

H. Sugiyama
Institute for Integrated Cell-Material Sciences (iCeMS)
Kyoto University
Yoshida-ushinomiyacho, Sakyo-ku, Kyoto 606–8501, Japan

their interconnected networks. In nature, living organisms have evolved sophisticated photo-responsive systems based on specific enzymes and molecular photo-switches, such as channelrhodopsins.[6] Inspired by these natural photosystems, scientists have developed and ingeniously combined various molecular photo-switches that can be integrated with biomolecular structures, such as proteins and DNA. Integrating this approach offers the ability to manipulate the structural, functional, and behavioral properties of the biomolecules under investigation through a light-induced reversible transformation, allowing for precise control.[7,8]

For instance, the light-dependent isomerization of azobenzene is a prime example of a synthetic photo-switchable system.[9] Azobenzene and its analogs have been widely used to modulate cellular functions and biochemical pathways, exploiting the photochromic properties between the stable E-isomer and the metastable Z-isomer. Photo-controllable DNA nanodevices, combining azobenzene isomerization and DNA hybridization, have gained interest in DNA nanotechnology.[10–12] Nonetheless, azobenzene requires UV irradiation and high temperatures for efficient photo-switching, and its short thermal half-life limits its bio-applications.[13,14] To overcome these limitations, Fuchter et al. recently reported AAPs as photochromic molecules with quantitative photo-switching and long thermal half-lives.[14,15] AAPs show promise for biological systems and expand the available photoswitches for DNA and nanomaterial-based systems, particularly those constrained by biological microenvironments and strict DNA sequence designs.[10,15–17]

While these advancements are promising, traditional photo-responsive bio-manipulation techniques rely on UV light, which has inherent limitations due to phototoxicity and limited penetration depth in biological applications.[18] Light scattering and off-target absorption reduce the effectiveness of these techniques in deeper tissue layers. To overcome these challenges, researchers have used lanthanide-doped upconversion nanoparticles (UCNPs). UCNPs are a unique class of optical nanomaterials doped with lanthanide ions, featuring multiple electronic transitions within their 4f electron shells.[19] These nanoparticles can upconvert two or more lower-energy photons into one high-energy photon, enabling them to emit specific wavelengths in the UV-vis region when excited by NIR light. This anti-Stokes photo-physical characteristic of UCNPs has gained traction and shown immense potential in various bio-applications.[20–22] Compared to other nanomaterial-based fluorescent vectors, UCNPs offer distinct advantages, including weak background signals, extended luminescence lifetimes, and superior photostability, making them well-suited for bio-applications.[23,24] UCNPs have shown promise in molecular imaging, photodynamic therapy, drug delivery, and optogenetics.[25–28] Recently, our team and others have demonstrated NIR-responsive drug release using UCNPs functionalized with photosensitive molecules. For instance, we developed a nano-construct based on UCNPs for the remote control of stem cell differentiation. This construct utilizes photosensitive poly-spiropyran moieties to precisely control the delivery of retinoic acid to NSCs. By harnessing the unique properties of UCNPs, we can achieve targeted and efficient drug release in response to NIR light, allowing for the modulation of NSC differentiation pathways with high spatiotemporal precision. This innovative approach highlights the potential of UCNP-based systems in advancing stem cell research and therapeutic applications by providing a versatile and minimally invasive method for controlling stem cell fate in complex biological environments.[29,30]

To address the critical challenges in spatiotemporally controlled drug delivery for stem cell research, we developed a hybrid DNA nanostructure-based NIR photo-switching system (**Figure 1A**). This system is combined with novel photochromic molecules, specifically AAP derivatives, to achieve precise control over stem cell neuronal differentiation. Azobenzenes, while widely used for photo-switching, often suffer from limited thermal stability of the cis isomer, leading to challenges in maintaining the desired drug delivery state. In contrast, our developed AAP photochromic molecules demonstrate superior performance with higher switching efficiency (≈98%, even after multiple switching cycles) and significantly enhanced cis form stability (Z to E transformation half-life extended to 1000 days).

To further enhance this approach, we constructed a NIR-mediated spatiotemporal DDS by combining AAP-containing DNAs with UCNPs. A set of AAP derivatives, including newly generated motifs, were designed and successfully synthesized via condensation reaction with a backbone scaffold for the solid-phase oligonucleotide synthesis. The UCNP multi-shell structure with 980 nm-sensitizers was synthesized for the advanced delivery system. The core of the UCNP is a hexagonal ß-phase $NaYF_4$ matrix doped with ytterbium (Yb^{3+}) for 980 nm sensitization and thulium (Tm^{3+}) for activation and subsequent photon emission in the UV region. The shell of the UCNP comprises inert $NaYF_4$ for surface passivation, followed by a final silica (SiO_2) shell for aqueous stability and DNA conjugation. Next, 5′-end thiolated DNA sets were covalently attached to UCNPs via thiol-maleimide reactions. Two complementary DNA strand conjugated UCNPs were prepared and hybridized for the small molecule loading (Figure 1B).

To achieve our goal of spatiotemporal control over the differentiation of NSCs, we selected curcumin, a molecule known for its neurogenic properties. Curcumin, a natural polyphenol, demonstrates anti-inflammatory, neuroprotective, and neurogenic benefits and can also bind to DNA's minor groove. Curcumin is widely recognized for its potent ability to stimulate neurogenesis by activating the Wnt/β-catenin signaling pathways. This phenomenon has been substantiated in both human cell cultures and animal models.[31,32] It shows neuroprotective effects in diseased animal models by inhibiting amyloid-ß generation through autophagy induction via PI3K/Akt/mTOR signaling downregulation in neurons.[33] Curcumin promotes the proliferation and differentiation of various stem cells, including neural progenitors.[34–36] Additionally, it has also been reported to induce neurite outgrowth during neurodifferentiation. It activates Wnt signaling pathway genes in neurons, regulating NSC proliferation and differentiation in the hippocampus.[37] Although not fully understood, curcumin likely inhibits GSK-3ß within the Wnt/ß-catenin pathway, leading to increased cytosolic ß-catenin and activated gene transcription. By activating the Wnt/ß-catenin pathway and providing a neuroprotective environment, we believe curcumin can effectively enhance NSC development and differentiation spatiotemporally.

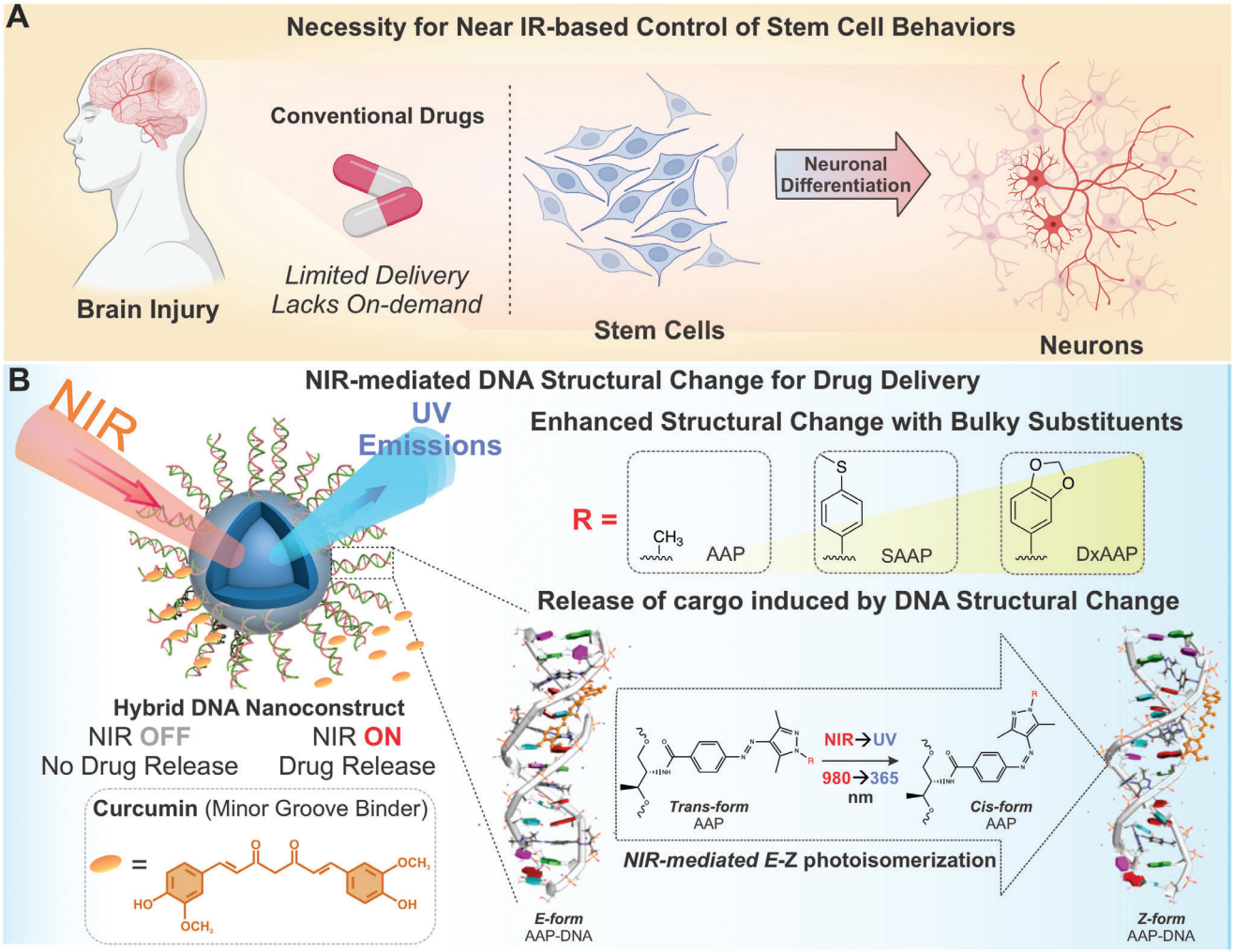

Figure 1. Photo-switching DNA nanoassembly for NIR-mediated modulation of cell fate. A) Schematic diagram displaying the necessity for remote control stem cell differentiation techniques relative to traditional approaches using conventional drugs. B) Schematic diagram of the constructed NIR-mediated photo-switching drug delivery system for the remote-control differentiation of NSCs. Left: NIR-mediated curcumin release is induced by NIR-to-UV photon upconversion in a photo-controllable manner. Curcumin is bound in the minor groove of the synthesized DNA construct containing the AAP photo-switcher. Right: The rational design of several AAP molecules with substituents varying in size led to increased DNA-duplex destabilization upon NIR irradiation, allowing the controlled release of curcumin from the DNA construct.

Ultimately, this nano-drug delivery system (NDDS) was delivered to NSCs with the goal of enhanced neurodifferentiation. Upon exposure to NIR light, the functionalized UCNPs efficiently converted low-energy NIR light into high-energy UV light. This up-conversion emission triggered photoisomerization in the AAP photo-switches from their trans-state to their cis form, leading to the dissociation of the DNA duplex. As a result, curcumin was released, enabling targeted gene modulation. By leveraging this photo-switching mechanism, we developed a novel and effective technique for the spatiotemporal regulation of NSC differentiation. Our NIR-mediated photo-switchable NDDS offers a precise and innovative approach to control stem cell fate. In short, our developed platform technology and method hold great potential across various fields, including nanomedicine, neuroscience, and regenerative medicine, promising future advancements and applications.

2. Results

2.1. Design and Synthesis of Novel Photoswitching Analogs for the Control of Duplex Hybridization

The facile synthetic access is one of the advantages that make AAP an attractive module for various applications. Structural manipulation of a substituent on a five-membered heterocycle allows for fine-tuning photoswitching behavior. In this study, we designed and synthesized new AAP derivatives containing 3-(methylthio) phenyl and 3,4-methylendioxy on *N*1-pyrazole (**Figure** 2A). Adding a methylthio group is anticipated to reduce the energy (resulting in a longer wavelength) needed for the E to Z transformation due to its electron-donating property.[38] In addition, incorporating a sterically bulky functional group or a heteroatom with electronic repulsion is anticipated to facilitate DNA

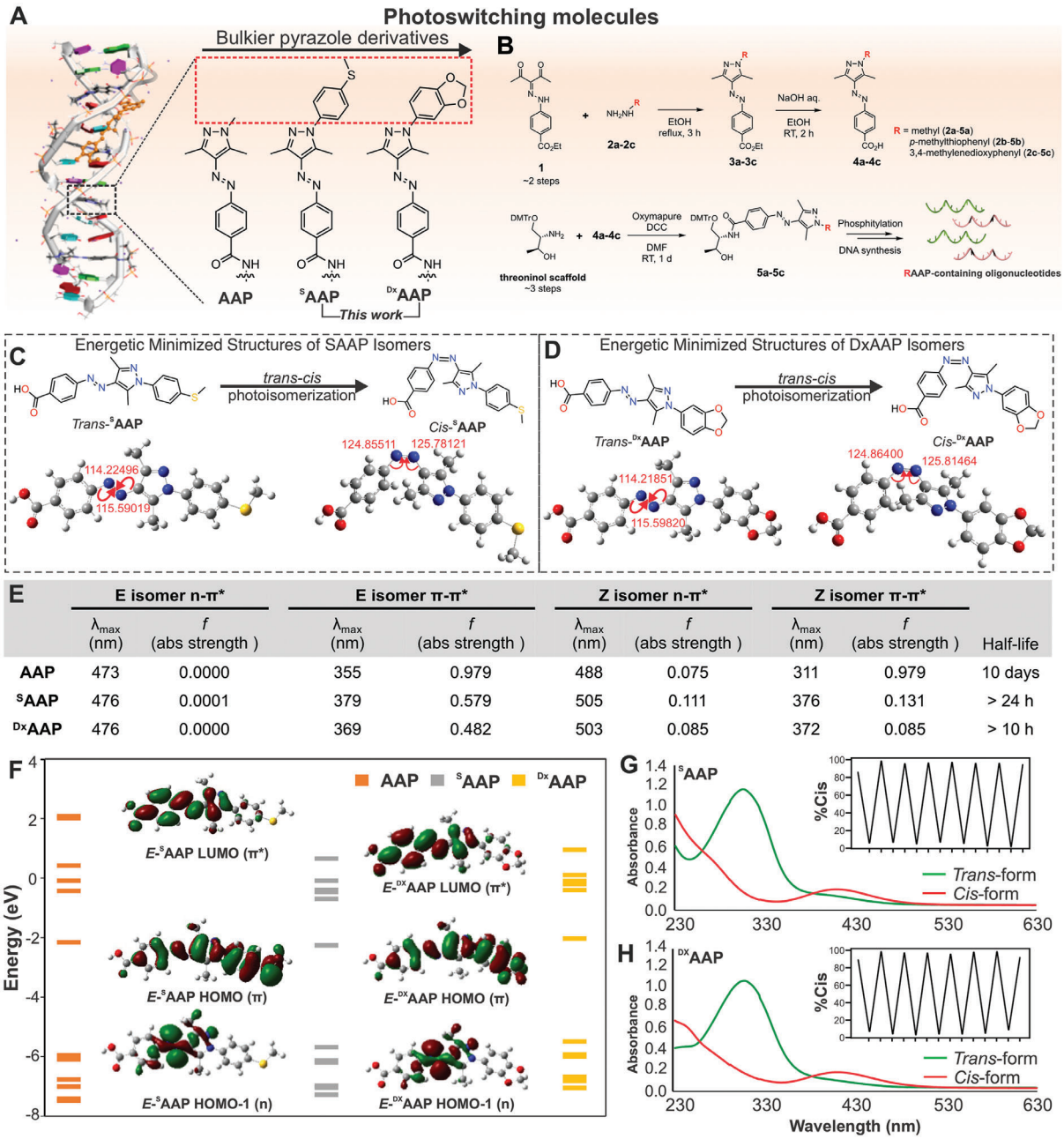

E

	E isomer n-π*		E isomer π-π*		Z isomer n-π*		Z isomer π-π*		
	λ_{max} (nm)	*f* (abs strength)	λ_{max} (nm)	*f* (abs strength)	λ_{max} (nm)	*f* (abs strength)	λ_{max} (nm)	*f* (abs strength)	Half-life
AAP	473	0.0000	355	0.979	488	0.075	311	0.979	10 days
SAAP	476	0.0001	379	0.579	505	0.111	376	0.131	> 24 h
DxAAP	476	0.0000	369	0.482	503	0.085	372	0.085	> 10 h

Figure 2. Design and Synthesis of Arylazopyrazole-based Photoswitching Molecules. A) Several AAP derivatives containing bulkier moieties for increased DNA-duplex destabilization. B) Synthetic scheme of AAP-based derivatives and their integration into the backbone of a DNA construct. C) Energetic minimized structures of SAAP in trans and cis configurations. D) Energetic minimized structures of DxAAP in trans and cis configurations. E) TD and DFT calculations for each AAP derivative displaying associated lambda max and absorbance strength values, in addition to half-life for the isomerization. F) Energy diagrams of AAP, SAAP, and DxAAP with associated HOMO and LUMO orbitals. G,H) Displaying UV–vis measured photoisomerization of SAAP and DxAAP molecules between trans and cis configurations.

conformational changes through the E to Z transformation. The synthetic scheme of AAP and S/DxAAP are shown in (Figure 2B). (*E*)-arylazopyrazoles possessing each different substituent (**3a–3c**) were obtained via a ring formation reaction between ethyl-*p*-(acetylacetobylidenehydrazino) benzoate (**1**) with hydrazine precursors (**2a–2c**). De-esterification and subsequent condensation reactions were performed to get DMTr-protected D-threoninol conjugates (**5a–5c**). The characterized S/DxAAP building blocks were then phosphorylated and applied to solid-phase DNA synthesis without further purification procedures. (Detailed synthetic procedures are described in the Supporting Information)

To verify its performance as a photoswitching molecule, we characterized the photophysical features of the newly designed SAAP and DxAAP. We measured UV/Vis spectroscopy with

compounds **4b** and **4c** (Figure 2G). Without UV irradiation, the AAP derivatives primarily exist as thermodynamically stable *E*-form isomers. The absorption maxima of ^{S}AAP and ^{Dx}AAP were slightly red-shifted to 373 nm and 366 nm compared to the conventional photo-switching AAP. After we optimized the wavelength for the photo-isomerization, it was found that the E to Z transformation readily occurred within 1 min of irradiation at the corresponding wavelength (≈400 nm for ^{S}AAP and ≈390 nm for ^{Dx}AAP). As shown in Figure 2G,H, we repeatedly observed quantitative E to Z isomerization of ^{S}AAP and ^{Dx}AAP for over six cycles. Rapid, efficient, and reversible photo-isomerization suggests that the newly devised AAP derivatives can be comparable to or outperform the original AAP molecule.

Next, we conducted a DFT/TD-DFT calculation to understand the effects of the structural modification of AAP on spectral features and photoswitching behavior (Figure 2C–F). We derived the optimized geometry of the photoswitching molecules using B3LYP/6-31G(d) density functional theory (DFT) calculations. The coordination scan of the dihedral (-C-N = N-C-) was executed from -60^0 to 60^0 and plotted. The energy level of each configuration suggests that the planner *E*-isomer was the most stable form. Thus, the planar structures for all (*E*)-AAP derivatives were obtained with annotated C-N = N angles. The minimized structures of (*Z*)-$^{S/DX}$AAP were found to have a dihedral angle of 12.8^0, with similar conformation to conventional AAP (12.9^0), indicating that the nitrogen substitution at pyrazole did not alter the essential structural characteristic of native AAP. The energy diagram, as well as HOMO and LUMO orbitals, are depicted in (Figure 2F). We set the energy relationship with HOMO-1 (n), HOMO (π), and LUMO (π^*) and calculated the HOMO-LUMO gap for each molecule. Conventional azobenzenes typically relied on UVA irradiation for trans (E) to cis (Z) isomerization through a π–π^* transition, whereas arylazopyrazole (AAP) derivatives narrow the energy gap of the n → π^* and π → π^* electronic transitions, resulting in a red-shift in the absorption spectra. In the present DFT/TD-DFT calculation, the energy gap between the HOMO and LUMO for $^{S/Dx}$AAP has narrowed due to an increase in the HOMO level and a decrease in the LUMO level. This supports that the E isomer of AAP derivatives can be switched at the longer wavelength because π → π^* electronic transitions are tolerant. It is consistent with previous computational studies and the competent photoswitching behavior of newly designed $^{S/Dx}$AAP.

2.2. In Silico Design of Functional DNAs for Generating a Photo-Controllable and Photo-Switchable DNA Library

Introducing chemical modifications with functional groups to natural oligonucleotides can enhance their properties, significantly broadening their potential applications. We have established a systematic modular strategy combined with a computational modeling study for the chemical modification of oligonucleotides.[15–17] A comprehensive array of functionalized DNA sequences has been achieved by strategically grafting various functional groups into specific locations on the oligonucleotides. The successful demonstration of DNA metalloenzymes and light-controlled phase separation using functionalized oligonucleotides has motivated us to further investigate the development of photo-switchable nanostructures and photo-responsive biomaterials through a modular approach.[39–43] To this end, AAP-functionalized oligonucleotides were designed as photoswitching DNA nanodevices for drug delivery. The phosphoramidites of AAP and $^{S/Dx}$AAP building blocks (**5a–5c**) were prepared and subsequently incorporated into the specific position on DNA strands via a solid-phase DNA synthesis procedure. Considering the operational efficiency of photoswitching DNA nanodevice, a series of AAP-functionalized oligonucleotides were synthesized by manipulating the position and number of AAP derivatives. As shown in (**Figure 3C**), we synthesized DNA oligonucleotides containing from one to three AAP derivatives. For the deployment of photoswitching, we decided to place AAP modules two bases apart from each other to ensure the stability of the overall DNA structure. Native DNA duplex without AAP modules (No AAP) was synthesized for comparative experiments. We demonstrated the responsiveness of the system by showing DNA structural deformations upon exposure to light, which was confirmed through thermal stability measurements. This corroborates the photo-induced dynamic behavior of the DNA construct. Furthermore, we evaluated the photo-responsivity of the AAP-modified DNAs. The efficacy of photo-regulation on the DNA strands can be gauged by the decrease in absorption intensity ≈360–370 nm range, as indicated in (Figure 3D). In conjunction with the experimental approach, we conducted a molecular modeling study to predict and gain insight into the conformational stability of AAP-modified DNA duplexes upon E to Z isomerization. As shown in (Figure 3A,B), energetically minimized structures indicate that the E-isomer of AAP introduced via threonine linker forms a stable helical structure by π–π stacking with DNA base pairs. In contrast, the introduction of Z-isomer induced the significant distortion of double helical structures, indicating dehybridization of the DNA duplex by photo-irradiation. It was found that increasing the number of AAP (2AAP and 3AAP) did not cause detrimental effects on the global DNA structures, remaining double helical structure, and shape of major/minor grooves. The plausible $^{S/Dx}$AAP-containing DNA structures by molecular modeling indicated that the presence of bulky substitutions reduced duplex stability (AAP>^{S}AAP>^{Dx}AAP for both E and Z). This destabilization by the steric hindrance may exert a beneficial effect on DNA dissociation. To elucidate the structural changes in the photo-switchable DNA nanodevice responsible for drug delivery, we performed a docking analysis on the DNA complex with curcumin. Curcumin is a well-known phenolic minor groove binder, and its binding mode has been investigated using native and synthetic oligonucleotides. Curcumin could be securely docked for the E-isomer AAP, spanning across 3 to 4 base pairs in the minor groove of the DNA duplex (Figure 3E). The ligand interaction diagram displays hydrophobic interactions between the aromatic curcumin group and the DNA binding site. On the contrary, in the case of the Z-isomer AAP, curcumin did not find a suitable binding site and became exposed due to the distorted helical structure.

2.3. Construction of NIR-Responsive Hybrid DNA Nanoconstructs for Controlled Drug Release

To achieve NIR-mediated DNA structural changes, we synthesized a core-shell-structured UCNP capable of absorbing NIR

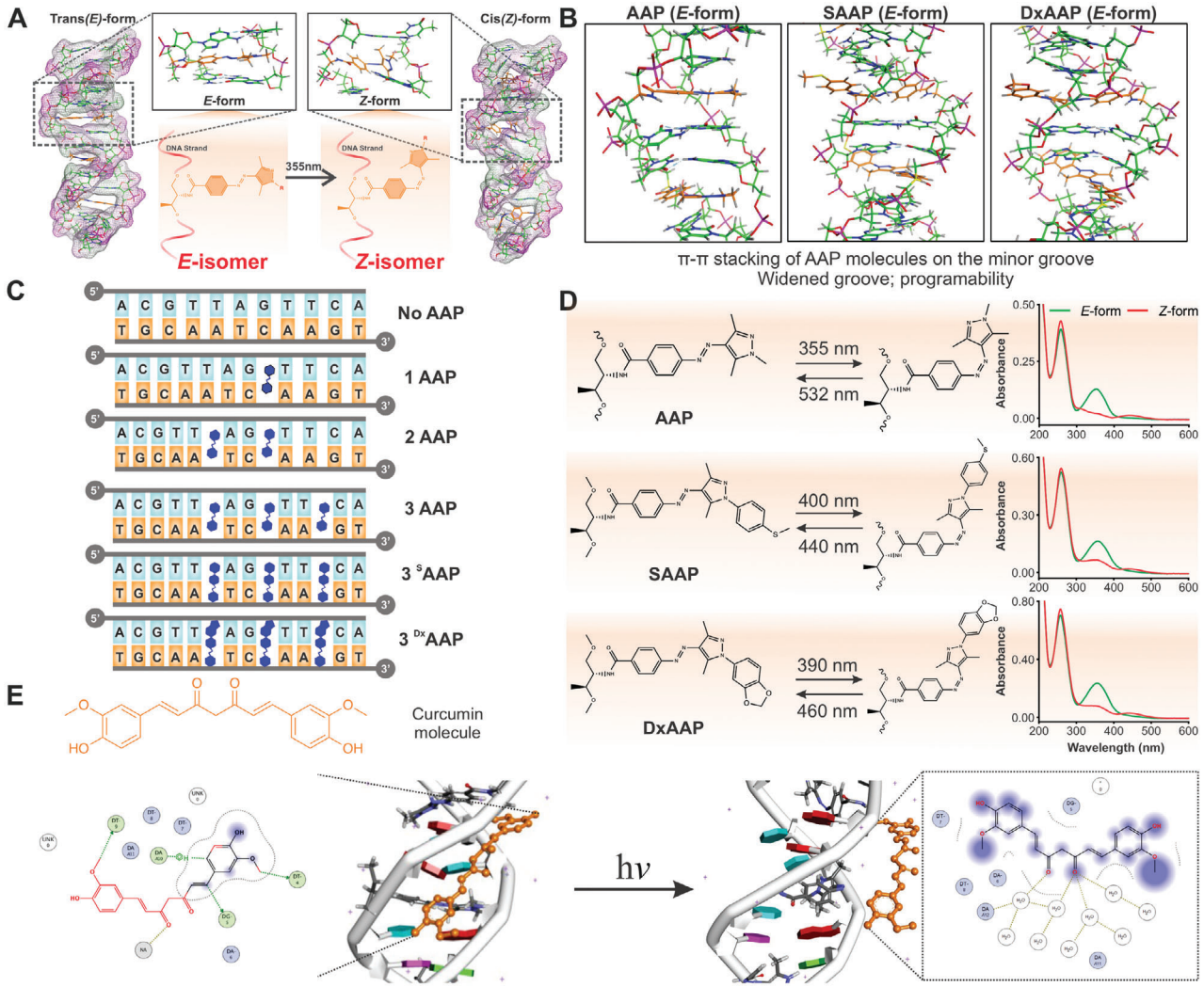

Figure 3. Photoswitching DNA nanodevice for NIR-mediated modulation of cell fate. A) Molecular modeling of synthesized DNA constructs containing an AAP derivative using an MOE software package. The space-filling model displays the shape and structure of the DNA construct stabilized and destabilized from AAP photoisomerization. B) Molecular modeling of synthesized DNA constructs containing each AAP derivative in its *E* configuration. C) Depiction of DNA sequences with varying numbers of AAP, ^{S}AAP, or ^{Dx}AAP molecules incorporated into the backbone. D) UV–vis measurements for E and Z configurations of AAP, ^{S}AAP, and ^{Dx}AAP molecules. E) Plausible curcumin binding models upon photoirradiation and ligand diagram interaction.

light at 980 nm wavelength and emitting UV/blue light within the excitable region of $^{S/DX}$AAP (≈325–375 nm). First, we wanted to maximize the likelihood and efficiency of the energy level transitions $^{1}I_6 \rightarrow {}^{3}F_4$ and $^{1}D_2 \rightarrow {}^{3}H_6$, which are responsible for the emissions peaks ≈345 and 363 nm, respectively.[44,45] Although it has been reported that incorporating a higher activator concentration can improve upconversion luminescence, specifically doping higher amounts of thulium (Tm^{3+}), this enhancement often comes at the expense of $^{1}D_2 \rightarrow {}^{3}H_6$ energy transitions in favor of $^{1}G_4 \rightarrow {}^{3}H_4$, which gives a larger 802 nm emission for a less intense 363 nm emission.[46–48] To this end, the core of the UCNP was chosen with these considerations in mind and was composed of a $NaYF_4$ host co-doped with 0.5 mol% Tm^{3+} and 20 mol% Yb^{3+}. Additionally, the epitaxial growth of an optically inert shell was implemented to act as a surface defect passivator and reduce the amount of Yb^{3+} atoms exposed to the surface, thereby mitigating surface quenching effects that result in non-radiative energy transfer (**Figure 4A**). Detailed characterization of the UCNP structure was performed using transmission electron microscopy (TEM), showing that the synthesized UCNPs displayed a uniform spherical/hexagonal shape with an average size of ≈55 nm (Figure 4B-1). The luminescence properties of UCNP were assessed to evaluate the efficiency of UV light emission, which is critical for triggering the AAP-mediated photoisomerization process, leading to the structural changes of the DNA and subsequent release of curcumin. Upon 980 nm NIR-light excitation, the UCL spectrum showed an emission within UV (λ_{max} = 344 and 360 nm) and visible (λ_{max} = 437 and 475 nm) regions (Figure 4C).

Prior to introducing photoswitching DNA onto the UCNP, the surface of UCNP was coated with a silica shell via co-condensation of tetraethyl orthosilicate (TEOS) and

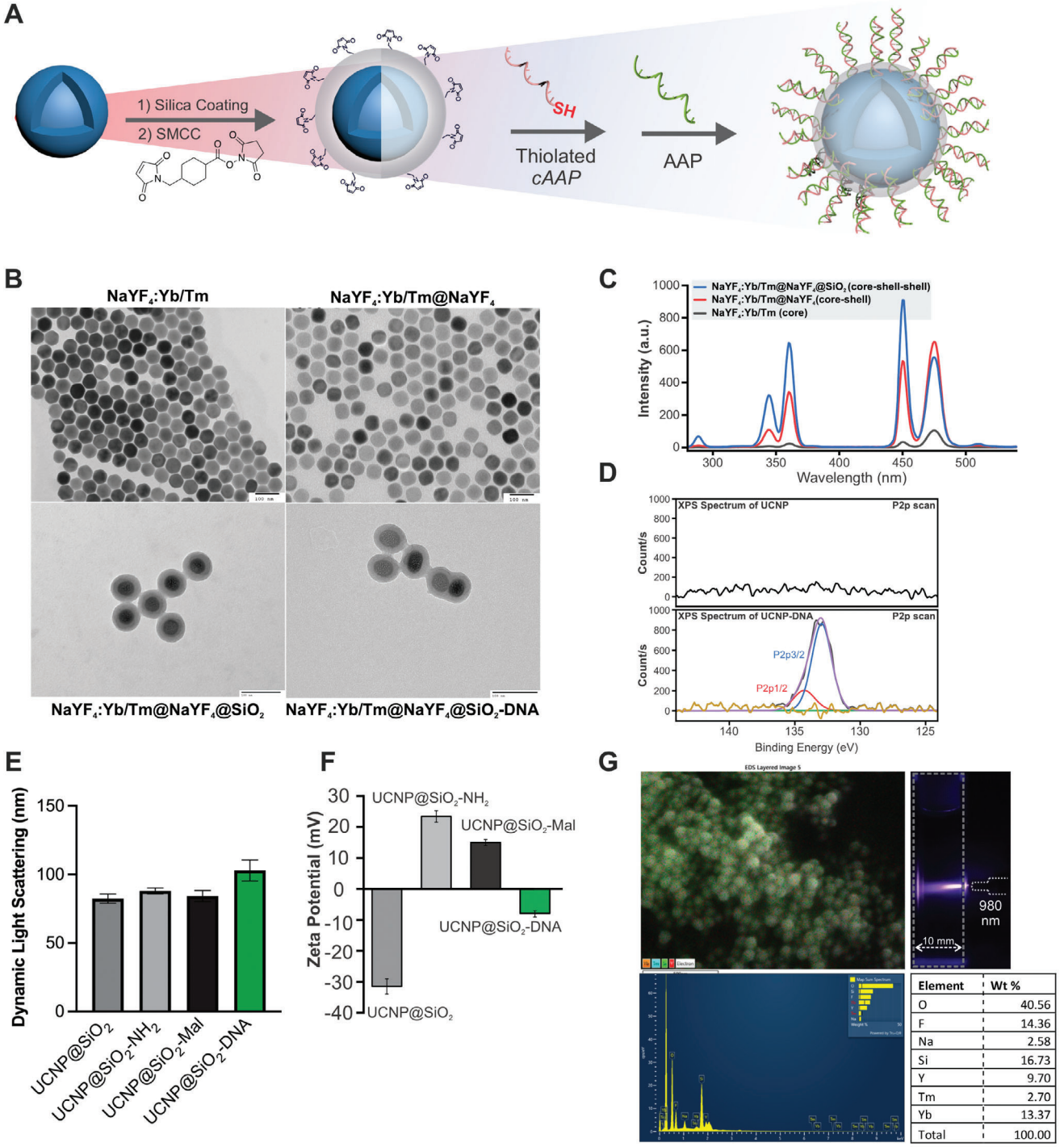

Figure 4. Construction of photoswitching DNA Nanoconstructs. A) Synthetic schematic for the assembly of the NIR-mediated photoswitching drug delivery system. B) TEM images of the synthesized UCNPs at different stages of assembly. C) Fluorescence measurements of $NaYF_4$:Yb/Tm, $NaYF_4$:Yb/Tm@$NaYF_4$, and $NaYF_4$:Yb/Tm@$NaYF_4$@SiO_2 respectively. D) XPS spectra of the UCNP with (bottom) and without (top) DNA on the surface, displaying the presence or lack of phosphorous content on the surface. E) DLS measurements of the synthesized UCNP after surface modification for DNA conjugation. F) Zeta potential measurements of the synthesized UCNP after surface modification for DNA conjugation. G) Top left: SEM-EDS image of $NaYF_4$:Yb/Tm@$NaYF_4$@SiO_2 with overlayed elemental mapping. Bottom left: Elemental map sum spectrum of elements detected in SEM-EDS image. Bottom right: Table of elements composition with corresponding weight percentage. Top right: Image of NIR-to-UV photon upconversion from 980 nm light irradiation.

(3-Aminopropyl) triethoxysilane (APTES). This surface modification aimed to introduce amino groups on the surface of the NP and enhance the particle stability in an aqueous environment. The silica coating resulted in monodisperse UCNPs with the size maintained at ≈84 nm, as measured by TEM (Figure 4B-3). Interestingly, the silica coating further enhanced the upconversion luminescence, specifically in the UV region, owing to the additional protective layer from energy transfer to the solvent (Figure 4C). Furthermore, SEM-EDS analysis was performed to investigate the elemental composition of the UCNPs after silica coating (Figure 4G). According to the elemental map sum spectrum and corresponding table, reasonable and predictable amounts of Yb^{3+} and Tm^{3+} were detected in the UCNPs. In addition, a uniform layer of silica was also observed on the surface of the UCNPs in the SEM images. To prepare the UCNPs for conjugation with thiolated DNA, the surface amino groups were modified with sulfosuccinimidyl 4-(N-maleimidomethyl) cyclohexane-1-carboxylate (Sulfo-SMCC) to introduce maleimide groups on the silica surface. Next, the thiolated oligonucleotides (complementary to AAP-containing oligonucleotides; cAAP) were grafted onto the UCNP@SiO_2-NH_2 via a thiol-maleimide "click" reaction, forming UCNP-cAAP. Subsequently, the AAP-containing oligonucleotides were annealed at 95 °C for 5 min and allowed to cool down to form UCNP-DNA-AAP nanoparticles (Figure 4A). The process of surface functionalization was verified by detecting a shift in zeta potential and an increase in size, measured by dynamic light scattering (DLS) (Figure 4E-F). The TEM images of the UCNP-DNA-AAP showed the homogenous coating of the DNA layer, contributing to an overall average size of ≈92 nm for the entire construct (Figure 4B-4). In addition, the XPS spectra confirmed the presence of DNA on the surface via the appearance of a phosphorus signal (P 2p3/2 and 2p1/2) (Figure 4D).

2.4. NIR-Mediated Modulation of Signaling Pathways in Biological Systems

Before studying the biological ramifications associated with our system, we took preliminary steps to fine-tune the intracellular delivery mechanisms for the UCNP-DNA-AAP constructs. We strategically functionalized the constructs with a cell-penetrating peptide (CPP) to enhance their ability to translocate across cellular membranes effectively. More specifically, we chose to incorporate the arginine-rich TAT peptide, which is derived from the Human Immunodeficiency Virus (HIV). This choice was motivated by the well-documented and superior capability of the peptide for penetrating cellular membranes, thereby serving as an effective vehicle for the intracellular delivery of our UCNP-DNA-AAP constructs.[49] It is worth noting that other targeting and bioactive molecules can be easily introduced to the UCNP platform via surface functionalization strategies. To quantify the transfection, we first conjugated a cyanine dye, Cy5, to the 5′-end of an oligonucleotide strand and introduced it onto the UCNP-DNA-AAP construct (**Figure 5E**). Human embryonic kidney 293 cells (HEK-293T) were used as a model for the assessment of UCNP-DNA-AAP cellular delivery. From flow cytometry, we observed that the fluorescent intensity of Cy5 in HEK-293T cells treated with TAT-conjugated UCNP-DNA-AAP had a significantly higher intensity than those without TAT conjugation (Figure 5F). The confocal microscopy confirmed the localization of Cy5-labeled UCNP-DNA-AAP inside the cells, while the Z-stacked image confirmed the intracellular delivery of our UCNP-DNA-AAP constructs (Figure 5G).

To assess the ability as a drug carrier, we loaded curcumin onto the duplex DNA structures of UCNP-DNA-AAP via DNA intercalation to the minor groove via π–π stacking and hydrogen bonding.[50,51] Our computational simulations have further confirmed these findings. Specifically, in the scenario where a stable isomer of DNA-AAP was formed, curcumin was observed to associate with the minor groove of the DNA structure. Moreover, adjacent nucleobases interacted electrostatically with the curcumin ligand, as depicted in (Figure 3E). Meanwhile, the simulations validated the photoisomerization process, facilitating curcumin displacement from the DNA structure and enabling its subsequent release into the surrounding microenvironment. Thus, our computational data robustly supports the concept of a light-reactive DNA assembly, providing a mechanism for the spatiotemporal release of the drug molecule. To test this mechanism experimentally, a kinetic NIR-mediated drug release assay was performed (Figure 5D). Upon NIR irradiation, conditions containing AAP-DNA (AAP, ^{S}AAP, and ^{Dx}AAP) displayed a burst-like release of curcumin that plateaued after irradiation was terminated. Interestingly, after washing the NPs following an incubation period with no NIR irradiation, further NIR exposure resulted in a second burst release of curcumin. This property was not observed in the control condition containing no photoresponsive AAPs (ØAAP). Therefore, it was confirmed that the UCNP-DNA-AAP systems were effective for the controlled release of curcumin in an aqueous environment. Specifically, both UCNP-DNA-^{S}AAP and UCNP-DNA-^{Dx}AAP conditions displayed significant levels of curcumin release in relation to UCNP-DNA-ØAAP, while UCNP-DNA-AAP did not. This result supports the hypothesis that bulkier substituents occupying the AAP molecule are more efficient at destabilizing the DNA duplex upon cis-to-trans photoisomerization in the NDDS, leading to a pronounced release of curcumin.

Curcumin is not only a suitable candidate for our study as a DNA minor groove binder, but it also possesses many biological properties, ranging from antitumor, antibacterial, and neurogenic functions.[52,53] In particular, we are interested in the biochemical property of curcumin to modulate the Wnt/β-catenin pathway.[54] Our engineered UCNP-DNA-AAP construct provides a promising platform for efficient and precise modulation of critical biological pathways. This is achieved by utilizing NIR light as a triggering mechanism, allowing targeted interventions in cellular processes with high spatiotemporal resolution. To evaluate the spatiotemporal modulation of Wnt/β-catenin using the UCNP-DNA-AAP platform, we employed a luciferase plasmid reporter containing the Wnt-regulating protein promoter, namely the T-cell factor/lymphoid enhancer factor (TCF/LEF) transcription factors. This allowed for the quantification of Wnt activity (Figure 5A). As shown in (Figure 5B), a significant increase in luciferase signal was observed upon NIR exposure, indicating the ability of our UCNP-DNA-AAP to function as a remote control for modulating specific signaling pathways owing to the controlled payload release. Subsequently, we aimed to investigate the effect of different levels of AAP

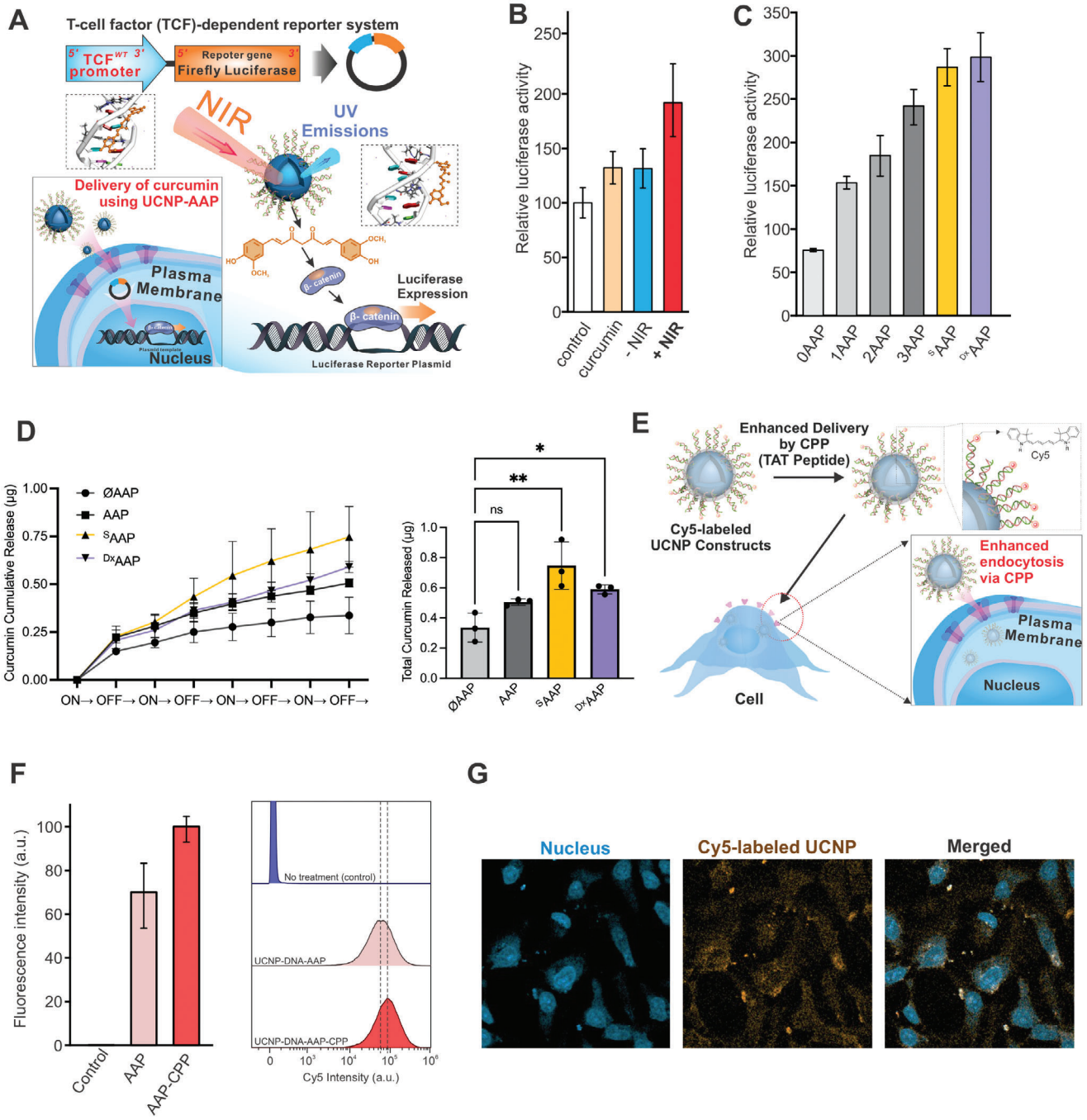

Figure 5. NIR-mediated Control of Wnt//β-catenin Signaling Pathways In Vitro. A) Schematic diagram of luciferase plasmid reporter containing the Wnt-regulating protein promoter, namely the T-cell factor/lymphoid enhancer factor (TCF/LEF) transcription factors. B) Relative luciferase fluorescence between control, free curcumin, UCNP-DNA-AAP construct with no NIR, and UCNP-DNA-AAP construct with NIR conditions, respectively. C) Relative luciferase fluorescence for varying AAP and AAP-derivative substitutions in the DNA duplex within the UCNP construct. D) Left: Kinetic NIR-mediate curcumin release assay for UCNP-DNA-ØAAP, UCNP-DNA-AAP, UCNP-DNA-^{S}AAP, and UCNP-DNA-^{Dx}AAP. "On" and "off" regions correspond to 3-min intervals with or without 980 nm NIR irradiation. Right: End-point total curcumin release for each condition, one-way ANOVA ($n = 3$, $^{*}p < 0.05$, $^{**}p < 0.01$). E) Schematic diagram displaying cellular uptake mediated by the cell-penetrating peptide TAT. F) Flow cytometry data of Cy5-labeled UCNP-DNA-AAP constructs internalized by HEK293T cells with and without assistance from TAT peptide. G) Immunofluorescence imaging of Cy5-labeled UCNP-DNA-AAP internalized by HEK293T cells with live NucBlue staining.

substitution on the degree of biological modulation. Specifically, we hypothesized that the number of AAP substitutions on the oligonucleotide sequences, ranging from one to three as illustrated in (Figure 3C), would directly affect the ability of the DNA duplex to release curcumin in response to structural changes induced by NIR light exposure.

As expected, the results indicated that the higher number of AAP substituents correlated with the higher luciferase activity when exposed to the NIR light (Figure 5C). Our hypothesis is supported by these results, which suggest that a higher number of AAP induces more significant structural distortion of DNA, resulting in a higher drug release efficiency in HEK-293T cells via different degrees of Wnt/β-catenin modulation. The structural effect of $^{DX/S}$AAP (i.e., the bulkiness of pyrazole derivatives) also played a role in the drug release efficiency of UCNP-DNA-AAP, as noticed from the release efficiency from AAP and $^{DX/S}$AAP-containing UCNP-DNA to the luciferase activities (Figure 5C), agreeing with the calculation performed in (Figure 3B).

2.5. NIR-Controlled Neuronal Differentiation Using Hybrid DNA Nanoconstruct-Based DDSs

To demonstrate the use of UCNP-DNA-AAP for NIR-mediated regulation of stem cell fate, ReN cells were treated with UCNP-DNA-AAP loaded with curcumin, followed by 980 nm light exposure (1.05 W cm^{-2}) for 9 min (3 min exposure intervals) before undergoing neuronal differentiation (**Figure 6**A). Initially, to find the optimal concentration for treating the ReN cells without inducing cytotoxic effects, cell viability assays were performed using a PrestoBlue reagent (Figure S13, Supporting Information). After 5 or 7 days of culture, we performed immunofluorescence imaging and quantitative polymerase chain reaction (qPCR) analysis, respectively, to evaluate the degree of neuronal differentiation (Figure 6B). The cellular uptake of UCNP-DNA-AAP in ReN cells was confirmed using flow cytometry (Figure 6D). Consistent with the results in HEK293T cells, we observed that ReN cells treated with Cy5-labeled and TAT-conjugated constructs showed a higher average intensity of cellular Cy5 signals compared to the control construct without TAT conjugation.

In this study, we were interested in demonstrating that our UCNP-DNA-AAP is an effective tool for precise and tunable controls of neurogenesis using NIR light. The immunostaining results did not yield overall significant differences between the expression levels of early and late neuronal markers, neuron-specific class III β-tubulin (TUJ1), and microtubule-associated protein 2 (MAP2), respectively (Figure 6E). However, we observed striking alterations in neuronal morphology within the groups treated with the UCNP-DNA-$^{S/Dx}$AAP conditions, starkly contrasting the changes in the ØAAP group. These morphological shifts in the neuronal structure provided compelling evidence for the efficacy of our engineered UCNP-DNA-AAP system in modulating biological processes. The morphological change, especially the neurite outgrowth, indicated neuronal lineage commitment (Figure 6F). Additionally, significant differences were not only found between AAP groups of increasingly bulky substituents but also between irradiated and non-irradiated conditions. Expanding on these results, further immunostaining was conducted to assess the morphological differences between the conditions with a higher cell-seeding density. The treated differentiating neurons were stained with synapsin-1 (synapsin) to visualize the synaptic density and neurite outgrowth between irradiated and non-irradiated conditions (Figure 6C). In general, higher levels of synaptic density and neurite outgrowth was observed in irradiated conditions, while all non-irradiated conditions appeared similarly. We investigated the TUJ1 mRNA expression level characterization through qPCR to further evaluate the effect of AAP substitution and structures for tunable gene expression. We observed an increasing trend of TUJ1 mRNA levels when the AAP substitution degree increases (Figure 6G), consistent with the Wnt luciferase assay performed in HEK293T. As expected, the TUJ1 mRNA level of AAP was significantly lower than those of $^{DX/S}$AAP. Interestingly, we did not see a significant difference in the mRNA level between ^{DX}AAP and ^{S}AAP. This observed outcome can be attributed to the varying quantities of curcumin released from the two distinct AAP motifs, which did not exhibit significant differences in their respective amounts. This hypothesis gains further credibility from our computational results, which consistently indicate that the number of AAP substitutions does not substantially alter the curcumin release profile.

To further evaluate the maturity and functionality of the differentiated neurons, the experimental groups were maintained under differentiation conditions with their associated treatment for up to 14 days. To characterize the functionality of the differentiated neurons, we performed calcium imaging to test their response to potential differences (Figure 6H). In particular, using a calcium indicator (Fluo-4), the corresponding intracellular calcium ion fluctuations were monitored. We quantified fluorescence changes and spontaneous fluctuations of calcium ions in the experiment group over 90 s, while the inactive control neurons showed minimal fluorescence intensity changes (Figure 6I). A recent study has shown that low-power blue illumination generated from UCNPs can activate the melanopsin/TRPC6 pathway and promote NSC differentiation into glial cells instead of neurons in a nongenetic manner.[55] This finding further necessitates our UCNP-based approach for NIR-mediated NSC differentiation into functional neurons.

3. Discussion

A wide range of tools have been developed using various biocompatible materials to manipulate intracellular dynamics and molecular mechanisms. Nanomaterial and DNA-based assemblies have been particularly powerful scaffolding options due to their inherent advantages, including high levels of multifunctionality, programmability, and synthesizability. In addition, multifunctionality allows for multiple actions or effects within a single construct, programmability enables customization of the structures to perform specific functions, and synthesizability indicates they can be readily manufactured using existing biochemical techniques. We have synergistically integrated two core research domains to advance this field by engineering a NIR-triggered NDDS. This system, composed of UCNPs and photo-switchable DNA constructs aided by novel AAP analogs, forms the UCNP-DNA-AAP. The integration of these components enables the spatiotemporal release of curcumin, which facilitates the differentiation of neural stem cells. This innovative

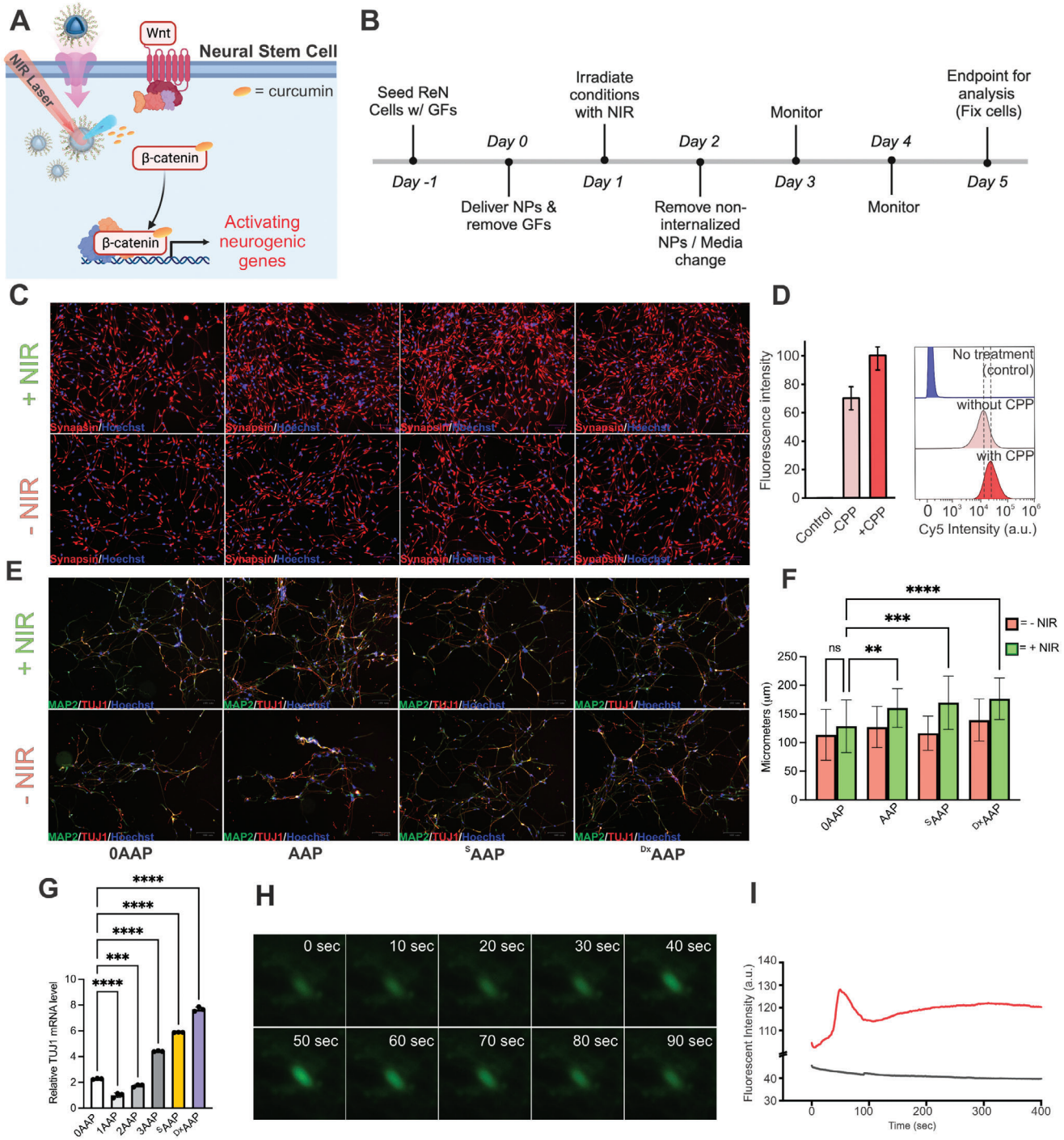

Figure 6. NIR-mediated control of neuronal differentiation via a Photoswitching DNA Nanoconstructs. A) Schematic diagram of the mechanism of curcumin-mediated Wnt/ß-catenin signaling activation in neurons. B) Timeline of enhanced neurodifferentiation experiment in ReN cells. C) Immunofluorescence imaging of ReN cells after UCNP-DNA-AAP treatment and 5 days of differentiation. Scale bar: 100µm. (Blue: Nucleus (Hoechst 33342). Red: Synapsin-1 (Synapsin).) D) Flow cytometry data of Cy5-labeled UCNP constructs internalized by ReN cells with and without assistance from TAT peptide. E) Immunofluorescence imaging of ReN cells after UCNP-DNA-AAP treatment and 5 days of differentiation. Scale bar: 100µm. (Blue: Nucleus (Hoechst 33342). Green: Microtubule-associated protein 2 (MAP2). Red: ß Tubulin (TUJ1).) F) Neurite outgrowth analysis of ReN cells after UCNP-DNA-AAP treatment and 5 days of differentiation, one-way ANOVA ($n = 3$, $^{*}p < 0.05$, $^{**}p < 0.01$, $^{***}p < 0.001$, $^{****}p < 0.0001$) G) Intracellular mRNA levels of TUJ1 in each condition quantified by qPCR, one-way ANOVA ($^{*}p < 0.05$, $^{**}p < 0.01$, $^{***}p < 0.001$, $^{****}p < 0.0001$) H) Spontaneous calcium fluctuations determined by Fluo4 fluorescence in ReN cells over 90 s of imaging. I) Fluorescent intensity of Fluo4 measured over time for calcium fluctuations in ReN cells.

approach combines the cutting-edge capabilities of nanotechnology and molecular biology, offering a highly precise and controllable platform for targeted therapeutic interventions. Building upon our well-established UCNP platform, we further expanded its utility by integrating it with DNA nanotechnology. This advancement overcomes the limitations faced by previous photoswitchable DNA nanostructures, which required the use of biohazardous UV light and less efficient azobenzene photoswitching molecules.

For this purpose, we designed DNA nanostructures with various AAP modules and analyzed their stability and secondary structure. Despite some structural distortions, all double-stranded DNAs containing 1–3 AAPs formed stable duplexes, confirmed by UV-melting assays. Higher AAP substitution increased photoisomerization efficiency and led to strand dissociation, while a 4th AAP reduced overall duplex stability due to excessive nucleobase replacement. Two novel photoswitching molecules, ^{Dx}AAP and ^{S}AAP, were synthesized by modifying N1-pyrazole with 3,4-methylenedioxy and p-(methylthio)phenyl groups. They formed stable π–π stacking interactions with neighboring nucleobases in the trans configuration. They exhibited enhanced photo-physical properties compared to conventional AAPs: high photoswitching efficiency, longer excitation wavelengths, and improved stability. This amplified their effectiveness as light-responsive scaffolds. Although we red-shifted photoisomerization wavelengths to 400 nm, UV light was still necessary for DNA-duplex destabilization. We used Yb^{3+} and Tm^{3+} doped UCNPs to convert 980 nm NIR light into UV wavelengths (345 and 360 nm) to trigger AAP photoisomerization. Once the system was assembled, 980 nm NIR light was used remotely to induce a NIR-responsive and controllable release of curcumin. In this way, UCNPs can potentially revolutionize nucleic acid-based delivery by efficiently delivering payloads to target cells. Furthermore, they offer the advantage of enhanced tissue penetration, which is crucial for effective therapeutic applications while minimizing photodamage. Neuro-differentiation in ReN cells using our UCNP-DNA-AAP system yielded promising results. UCNP-DNA-AAP, UCNP-DNA-^{S}AAP, and UCNP-DNA-^{Dx}AAP treatments significantly increased TUJ1 mRNA levels by day 7 compared to controls. Although curcumin treatment accelerated neurodifferentiation, it did not enhance final expression levels due to the spontaneous differentiation of ReN cells triggered by the removal of bFGF and EGF. UCNP-DNA-AAP, UCNP-DNA-^{S}AAP, and UCNP-DNA-^{Dx}AAP treatments also improved neurite outgrowth by likely activating the MAPK/ERK pathway via curcumin delivery. Non-irradiated conditions showed no significant difference from controls, indicating selective and controllable drug delivery. Further studies are needed to fully elucidate the role of curcumin-enhanced neurodifferentiation of ReN cells, but this UCNP-DNA-AAP system has the potential for accelerated neurodifferentiation applications.

In summary, the rapid advancements in nanomaterials, particularly UCNPs combined with DNA-AAP constructs, can open up exciting possibilities for targeted drug delivery and therapeutic applications. These advancements provide novel mechanisms to deliver therapeutic agents with high specificity and efficacy. UCNPs are noteworthy for their ability to convert low-energy NIR light into high-energy UV or visible light, allowing deeper tissue penetration and reduced photodamage. The integration of DNA-AAP constructs with UCNPs enhances functionality, offering programmability and multifunctionality for precise delivery of nucleic acids and other therapeutic molecules. Our developed strategy has the potential to enable the spatiotemporal release of nucleic acid-based therapeutics, including microRNA (miRNA), small interfering RNA (siRNA), and antisense oligomers (ASOs). We achieved exceptional precision and control over therapeutic delivery by modulating NIR irradiation. This innovative platform allows researchers and clinicians to regulate cellular functions and fates with high accuracy, influencing complex biological processes and disease pathways. As this technology continues to develop and advance, it has the potential to make a significant impact on addressing medical challenges and ultimately improving patient outcomes. The precise targeting and control of therapeutic delivery can lead to breakthroughs in treating cancer, neurodegenerative diseases, and genetic disorders, minimizing side effects and enhancing efficacy. In conclusion, integrating UCNPs and DNA-AAP constructs represents a significant advancement in the development of NDDSs and nanomedicine as a whole. This approach broadens the scope of targeted drug delivery and paves the way for innovative therapeutic strategies, promising to revolutionize healthcare and improve patient outcomes.

4. Experimental Section

Detailed methods, synthetic procedures, and characterization of the compounds are described in the Supplementary Information.

Materials: Thulium (III) acetate hydrate, ytterbium (III) acetate hydrate, yttrium (III) acetate hydrate, ammonium fluoride, sodium hydroxide, oleic acid, 1-octadecene, and (3-aminopropyl)triethoxysilane (APTES) were purchased from Sigma-Aldrich Chemicals Co. and used as received. Methanol, ethanol, hexanes, tetraethylorthosilicate (TEOS), and Dulbecco's phosphate-buffered saline (PBS) were purchased from Thermo Fischer Scientific and used as received. Sulfosuccinimidyl 4-(N-maleimidomethyl)cyclohexane-1-carboxylate (Sulfo-SMCC) was purchased from Chem Impex Int'l Inc. and used as received. Curcumin was purchased from TCI and used as received.

Preparation of ^{S}AAP and ^{Dx}AAP: Precursors of [4-(methylthio)phenyl]hydrazine and 1,3-benzodioxol-5-ylhydrazine were obtained from aniline by $SnCl_2$/HCl reduction. And, DMTr-protected *D*-threoninol and Ethyl-4-(2-(2,4-dioxopentan-3-ylidene)hydrazono)benzoate (**1**) have been synthesized according to previous reports. The ring close reaction for generating pyrazole was performed by mixing hydrazine derivatives and compound 1 in EtOH, reflux. The amide bond formation between AAP carboxylic acid and the threoninol scaffold was done by Oxymapure/DCC coupling.

Oligonucleotide Synthesis: Solid-phase oligonucleotide synthesis was performed on an ABI DNA synthesizer (Applied Biosystem, Foster City, CA). DMTr-protected AAP (^{S}AAP/^{Dx}AAP) phosphoramidites were prepared based on our previous studies[ref] and incorporated into oligonucleotides without purification. 1AAP-4AAP and 3$^{S/Dx}$AAP were synthesized on solid support using **AAP** phosphoramidite (compound **5a**–**5c**) and commercially available $O^{5'}$-dimethoxytrityl -2′-deoxyribonucleoside $O^{3'}$-phosphoramidites. For the AAP-modified oligonucleotides, the coupling reaction time was elongated for 10 min. The AAP phosphoramidite could be incorporated into desired position with comparable yield to the ones obtained with standard phosphoramidite building blocks. Cleavage from the solid support and deprotection, followed by purification with Glen-Pak cartridges yielded the desired oligonucleotides. After HPLC purification (2–40% ACN in 20 mM TEAA (pH 7.0) buffer, flow rate of 3.0 mL min^{-1} using COSMOSIL 5C18 AR-II column), synthesized oligonucleotides were confirmed by MALDI-TOF MS using a Bruker microflex-KSII (Bruker Corporation, Billerica, MA) (Table S2, Supporting Information). DNA

concentrations were determined by using NanoDrop ND-1000 (NanoDrop Technologies, Wilmington, DE).

Spectroscopic Measurements: CD spectra of oligonucleotide solutions collected in 1 nm steps from 360 or 320 to 220 nm were measured using JASCO J-805LST Spectrometer in a 1 cm quartz cuvette. UV melting was conductedby measuring changes in absorbance at 260 nm as a function of temperature. Absorbance was recorded from 5 to 90 °C at a rate of 1 °C min^{-1}. All samples were prepared in a total volume of 120 µL containing 5.0 µM oligonucleotide and 1x PBS buffer (pH 7.6).

Light Irradiation: For evaluating AAP molecules' photoswitchablity, purified compound **4a**–**4c** (100 uM in DMSO) was prepared in 1.5 mL brown eppen-dorf tubes. The samples were placed on the ice and irradiated 20 min with hyper monochromator (HM-5, Bunkoukeiki JAPAN, 8 W), various wavelength. For AAP-DNA irradiation, 10 uM of the modified DNAs in 1XPBS buffer (pH 7.6) was shined and directly transferred to UV spectrometer.

Quantum Mechanical Modeling: The geometry of AAP derivatives was optimized using DFT, and their optical parameter was calculated using TD-DFT methods as implemented in the Gaussian 16 W program package. All the calculations were done using B3LYP (Becke, three-parameter, Lee–Yang–Parr) hybrid exchange and correlation energy functional, default spin, with the 6–31G(d) basis set for all atoms. The DFT calculations were performed in the gas phase. After geometry optimization, frequency calculations were done to remove any vibrational unstable modes.

Macromolecular Modeling: Molecular modeling was carried out using the MOE (Molecular Operating Environment) 2019 software package. AAP-DNA and the complementary DNA duplexes were constructed and minimized with amber force field parameters, a distance-dependent dielectric constant of $\varepsilon = 4r$ (where, r is the distance between two atoms) and convergence criteria having an RMS gradient of less than 0.001 kcal mol^{-1} Å. For energy minimization water and salt molecules were added to produce distance of 10 Å from the solute to droplet sphere boundaries and sodium counter ions were added to neutralize the system.

Synthesis of $NaYF_4$:30%Yb,0.5%Tm (Core UCNP): The synthesis of Ln^{3+} doped $NaYF_4$ nanocrystals was performed by a modified procedure based on a protocol from Wilhelm et al.[1] Briefly, to a 50 mL round bottom flask, $Y(OAc)_3 \cdot xH_2O$ (0.695 mmol), $Yb(OAc)_3 \cdot xH_2O$ (0.3 mmol), $Tm(OAc)_3 \cdot xH_2O$ (0.005 mmol), oleic acid (6 mL) and 1-octadecene (16 mL) were added. The mixture was slowly stirred under argon flow and heated to 140 °C under vacuum for 30 min to obtain a clear solution. The flask was then cooled to 50 °C under argon and a solution containing NH_4F (4 mmol) and NaOH (2.5 mmol) in methanol (10 mL) was added with vigorous stirring and the suspension was held at 120 °C for 30 min under vacuum to remove volatile solvents before heating to 300 °C for 1.5 h. After the flask was cooled to room temperature, the particles were pelleted by centrifugation and washed with ethanol before being dispersed in 10 mL of hexane. Finally, large aggregates were removed by centrifuging the particles at 1000 g for 3 min and collecting the supernatant, which contains the Tm^{3+} doped seed particles.

Synthesis of $NaYF_4$:30%Yb,0.5%Tm@$NaYF_4$ (Core-Shell UCNP): The synthesis of the inert shell onto the Tm^{3+} doped seed particles was similar to the synthesis of the core. First, to a 50 mL round bottom flask, $Y(OAc)_3 \cdot xH_2O$ (0.9 mmol), oleic acid (6 mL) and 1-octadecene (16 mL) were added. The mixture was slowly stirred under argon flow and heated to 140 °C under vacuum for 30 min to obtain a clear solution. Later, the flask was cooled to 80 °C under argon and the Tm^{3+} doped seed particles were injected via syringe and heated to 90 °C to remove excess hexane. Then, the reaction was cooled to 50 °C and a solution containing NH_4F (3.61 mmol) and NaOH (2.25 mmol) in methanol (10 mL) was added with vigorous stirring and the suspension was held at 120 °C for 30 min under vacuum to remove volatile solvents before heating to 300 °C for 1.5 h. After the flask was cooled to room temperature, the particles were pelleted by centrifugation and washed with ethanol before being dispersed in 5 mL of hexane. Finally, large aggregates were removed by centrifuging the particles at 1000 g for 3 min and collecting the supernatant, which contains the core-shell particle.

Coating $NaYF_4$:30%Yb,0.5%Tm@$NaYF_4$ Nanocrystals with TEOS (UCNP@SiO_2): The coating of the core-shell nanocrystal was performed by a modified procedure based on a protocol for a reverse microemulsion by Jalil and Zhang.[2] Specifically, to a round bottom flask cyclohexane (15 mL) and Igepal CO-520 (2 µmL) were stirred for 10 min. Then, the $NaYF_4$:30%Yb,0.5%Tm@$NaYF_4$ nanocrystal (5 mg) was added to the mixture and allowed to stir for 10 min prior to the addition of ammonia hydroxide (105 L). TEOS (25 µL) was finally added to the mixture and left to stir at room temperature for 48 h. The silica-coated nanocrystals, $NaYF_4$:30%Yb,0.5%Tm@$NaYF_4$@SiO_2) were isolated by centrifugation and were washed three times with ethanol before being dispersed in 10 mL of ethanol.

Amine Functionalization of $NaYF_4$:30%Yb,0.5%Tm@$NaYF_4$@SiO_2 with APTES (UCNP@SiO_2-NH_2): The silica-coated nanocrystals were placed into a 25 mL round bottom flask and stirred prior to the addition of 120 µL of APTES. The amine-containing silane was allowed to graft onto the surface of the TEOS-coated particle for 24 h at room temperature prior to being centrifuged and washed three times with ethanol. These amine-coated nanocrystals ($NaYF_4$:30%Yb,0.5%Tm@$NaYF_4$@SiO_2-NH_2) were stored in ethanol at room temperature.

Maleimide Functionalization of UCNP@SiO_2-NH_2 with Sulfo-SMCC (UCNP@SiO_2-Mal): Initially, 5 mg of UCNP@SiO_2-NH_2 were centrifuged at 9000 rpm for 10 min and the resulting pellet was washed three times with distilled water to remove any residual ethanol from storage. After washing, the pellet was redispered in 1 mL of 0.1x PBS. Separately, 5 mg of Sulfo-SMCC was dissolved in 4 mL of 0.1x PBS and stirred in a 10-mL glass scintillation vial until dissolved. To this solution, 1 mL of UCNP@SiO_2-NH_2 (5 mg mL^{-1}, 0.1x PBS) was added drop-wise and left to react for 2 h. Once complete, this solution was transferred to a 15-mL conical centrifuge tube for centrifugation at 9000 rpm for 10 min. The resulting pellet was washed with copious amounts of water to ensure the removal of excess Sulfo-SMCC. Once washed, the UCNP@SiO_2-Mal was redispersed in 5 mL of 1x PBS to afford a 1 mg mL^{-1} solution. The stability of UCNP@SiO_2-Mal was much lower than that of UCNP@SiO_2-NH_2, so this solution should not be stored long-term.

DNA-AAP Functionalization of UCNP-SiO_2-NH_2 (UCNP-DNA-AAP): In a 1.5-mL Eppendorf tube, 20 µL of 10x PBS was diluted with 90 uL of nuclease-free water. To this, 1 µg of complimentary ssDNA (1 mg mL^{-1}) and 1 µg of ssDNA-AAP (1.3 mg mL^{-1}) were added. Once mixed gently, the tube was incubated at 95 °C in a heating block for 3 min. The tube was removed and set at room temperature for 5 min to help anneal the DNA-AAP. Next, 1 µL of (15 mM, DMSO) curcumin solution was added and after mixing gently, the tube was left stationary at room temperature for 10 min. To this solution, 100 µL of cold UCNP@SiO_2-Mal (1 mg mL^{-1}) was added to the tube with gentle pipetting to help mix. This mixture was left to gently shake at 4 °C overnight to ensure maximum conjugation. The next day, the tube was centrifuged at 9000 rpm for 10 min, affording an orange-tinted pellet which was subsequently washed with 100 µL of nuclease-free water. This centrifugation washing step was conducted a total of 3 times to ensure the removal of unreacted DNA-AAP and curcumin. Once washed, the pellet was redispersed in 100 µL of nuclease-free water to afford a concentration of 1 mg mL^{-1}. The UCNP-DNA-AAPs were stored at 4 °C for future experiments. For ^{S}AAP and ^{Dx}AAP conditions, the same procedure was followed with the replacement of ssDNA-AAP with the appropriate oligonucleotide.

Characterization of UCNP-DNA-AAP: Hydrodynamic diameter and zeta potential of the UCNP-DNA-AAP NPs were measured using a Malvern ZetaSizer Nano Series and NanoSight NS 3000 (Westborough, MA). For XPS analysis, 10 µL of the UCNP-DNA-AAP solution was dried on a cleaned silicon substrate and analyzed using a Thermo Scientific K-Alpha X-ray Photoelectron Spectrometer (XPS) System with a monochromated X-ray source (Al-Kα) and a base pressure of $<5 \times 10^{-8}$ mbar. TEM images of the UCNP-DNA-AAP NPs were acquired using a JEOL transmission electron microscope (JEM1010; JEOL, Japan) with an accelerating voltage of 80 kV. For SEM analysis, a field-emission scanning electron microscope (FE-SEM, Zeiss, Germany) was used to obtain morphology of the NPs, while energy dispersive x-ray spectroscopy (FE-SEM with the Oxford EDS detector) was used for elemental composition analysis. For FE-SEM with EDS, 15 µL of the purified NPs were drop casted onto carbon tape and dried overnight in a vacuum desiccator. The sample was coated with 15 nm

thick platinum using an ion sputter coater (KIC-1A, COXEM, South Korea) to form the conductive layer for SEM imaging and EDS analysis.

Kinetic NIR-Mediated Curcumin Release Assay: In a 1.5-mL Eppendorf tube, 150 µL of a 0.66 mg mL^{-1} solution of UCNP-DNA-AAP was clamped in place with the cap open. Directly above this tube (1-cm), a fiber-optic cable connected to a 980-nm laser was mounted and oriented to irradiate into the top of the tube. At a power density of 1.00 W cm^{-2}, the solution was irradiated for 3 min before being centrifuged at 9000 rpm for 10 min. Once centrifuged, 50 µL aliquots were removed and pipetted into three separate wells of a 96-well plate. Following, the resulting pellets were redispersed with 150 µL of DI water and incubated with no NIR irradiated for 3 min before being centrifuged again. Similarly, 50 µL aliquots were removed and pipetted into three separate wells adjacent to the previous aliquots. This process was repeated 4 times for a total of 12 min of NIR irradiation and 12 min of no NIR irradiation. Afterward, the 50-µL aliquots removed previously were all brought to 100 µL volume total with DMSO, affording 1:1 H_2O:DMSO aliquots. A six-point curcumin calibration curve was produced in 1:1 H_2O:DMSO with a concentration range from 50 µg mL^{-1} to 100 ng mL^{-1} ($R^2 = 1$). Absorbance values were measured in triplicate at 440 nm on a Tecan microplate reader, and the calibration curve was used to calculate the levels of cumulative curcumin release.

Cell Culture: Tissue culture vessels were coated with Matrigel (Corning) 1:200 dilution with Dulbecco's modified Eagle's medium (DMEM/F12) (Invitrogen) at 37 °C for 1 h. ReNcell VM Human Neural Progenitor Cell Line (ReNcells) were seeded onto the 10-cm Matrigel-coated plate (5×10^5 cells). ReNcells proliferated in a growth media containing DMEM/F12 with Glutamax (ThermoFisher Scientific), N2 Supplement (Thermo Fisher Scientific), 5 µg mL^{-1} gentamicin (ThermoFisher Scientific), and 20 ng mL^{-1} bFGF and EGF (Peprotech). The culture media was changed every other day with growth factors included until differentiation, at which point they were excluded from the media when changed.

Cell Viability Characterization: Cell viability assays were conducted in 96-well plates coated with Matrigel (Corning) 1:200 dilution with DMEM (Thermo Fisher Scientific) at 37 °C for 1 h. 20k of ReN cells in 100 µL of growth medium were seeded into each well. For nanoparticle concentration-dependent viability, increasing nanoparticle concentrations (0–100 µg mL^{-1}) were added into the well plate at day 1 for 24 h incubation. Subsequently, a resazurin-based viability reagent, PrestoBlue, was introduced into each well with 30 min incubation (day 2). Fluorescence intensity was determined using a Tecan microplate reader at 590 nm emission with 560 nm excitation. For NIR-intensity-based viability, an increasing 980 nm laser power density (0–8.42 W cm^{-2}) with irradiation diameter (6 mm) was applied to each well on day 1. The well plates were stored in an incubator for 24 h, followed by PrestoBlue-based viability assay, as described above (day 2).

980 nm NIR-Mediated Differentiation of Neural Stem Cells (NSCs): 980 nm NIR-mediated ReN cell differentiation experiments were conducted in 48-well plates, which were coated with Matrigel (Corning) 1:200 dilution with DMEM/F12 (Thermo Fisher Scientific) at 37 °C for 1 h. 15k of ReN cells in 200 µL of growth medium were seeded into each well. After 24 h with cell attachment on the culture plate, the culture medium and growth factors were removed and changed to nanoparticle constructs solution (10 µg mL^{-1} UCNP@DNA-AAP with loaded curcumin). After 24 h of incubation, the culture media was changed back to normal, but without bFGF and EGF growth factors. Once changed, "positive" wells were irradiated by a 980 nm laser at a power density of 1.00 W cm^{-2} for a total of 9 min, with 3-min intervals of "on" and "off". Treatment wells labeled "negative" received a treatment but were not irradiated. The cells were left undisturbed in the cell culture incubator from days 3–5 or 3–7, depending on the method of analysis to follow.

Immunofluorescence: In general, cultured cells were washed twice with DPBS (Thermo Fisher Scientific) and treated in formaldehyde solution (4%) for fixation for 20 min, followed by DPBS wash three times. Subsequently, the cells were permeabilized and blocked for nonspecific binding with blocking buffer containing 0.1% Triton X-100 and 5% normal goat serum (Life Technologies) in PBS for 1 h. To characterize the extent of neuronal differentiation, the cells were fixed, blocked, and stained with a primary mouse antibody against TUJ1 (1:500 dilution, Cell Signaling). Specifically, the fixed samples were incubated for 2.5 h at 4 °C in an antibody dilution buffer (PBS containing 10% NGS) with TUJ1 primary antibody. With three times PBS washing, the cells were incubated for 1 h (RT) in antibody dilution buffer containing Hoechst (3 µg mL^{-1}, Life Technologies) and anti-mouse secondary antibody labeled with Alexa Flour 594 (1:500, Life Technologies). Followed by three times PBS washing, the stained samples were visualized through a Nikon T2500 inverted fluorescence microscope. For a mature neuronal marker characterization, the primary rabbit antibody against MAP2 (1:500 dilution, Cell Signaling) was used. Subsequently, anti-rabbit secondary antibody Alexa Fluor 488 (1:500, Life Technologies) was utilized to visualize the mature neuronal marker through fluorescence microscopy.

Neurite Outgrowth Analysis: Images that were taken for immunofluorescence analysis were also used for neurite outgrowth analysis. Images of two fields per well were taken with roughly 100 cells per field. The neurite length of the differentiated ReN cells was measured for all identified neurite-bearing cells in a field by tracing the longest length of neurite per cell using the NeuronJ 1.4.3 plugin through Image J 1.53t software. Each experiment was conducted in triplicate. One-Way ANOVA statistical analysis was performed between experimental and control conditions using GraphPad Prism (Version 10.1.1).

Gene Expression Analysis: The expression levels of target genes were quantified by quantitative reverse transcription PCR (RT-qPCR) of mRNA extracted from tissue culture. The total RNA, including mRNA of interest, was extracted using TRIzol Reagent (Life Technologies). The total RNA (1 µg) was used as a template for a reverse transcription reaction to generate the first-strand complementary DNA (cDNA) using the Superscript III First-Strand Synthesis System (Life Technologies) according to the manufacturer's protocol. The first-strand cDNA was subsequently used for qPCR reaction with gene-specific primers in the presence of Power SYBR Green PCR Master Mix (Applied Biosystems) on a StepOnePlus Real-Time PCR System (Applied Biosystems). The output Ct values were normalized to GAPDH in triplicate, which was selected as the endogenous control. The standard cycling conditions were applied to all of the reaction conditions with a melting temperature of 60 °C.

Calcium Imaging: Differentiated neurons were incubated with 5 µM Fluo-4-AM (Life Technologies) media for 30 min. Subsequently, the treated cells will be washed with HBSS (Life Technologies) and incubated for 30 min in culture media for the deesterification process of the dye. The media was changed to HBSS for the initiation of the calcium imaging session. Under the movie mode of the Nikon Eclipse Ti-E microscope, a concentrated KCl solution in PBS (50 mM, 0.1 mL) was introduced into the neuron cultures. The video was captured at 60 frames per second imaging speed.

Supporting Information

Supporting Information is available from the Wiley Online Library or from the author.

Acknowledgements

T.P., J.H.Y., and C.D.M. contributed equally to this work. K.-B.L. acknowledges the partial financial support from the NSF (CBET-1803517), the New Jersey Commission on Spinal Cord (CSCR17IRG010; CSCR16ERG019), NIH 26 R01 (1R01DC016612, 1R01NS130836-01A1, 3R01DC016612-01S1, and 5R01DC016612-02S1), NIH RM1 (RM1 NS133003-01), NIH R21 (R21 NS132556-01), Alzheimer's Association (AARG-NTF-21-847862), CDMRP (OCRP, OC220235P1), N.J. Commission on Cancer Research (COCR23PPR007), and HealthAdvance (NHLBI, U01HL150852). S.P. appreciates the financial support by Grant-in-Aid for Transformative Research Area (A) [23H04076; "Material Symbiosis"]. This work was also supported by AMED under 22ama121025j0001 (Platform Project for Supporting Drug Discovery and Life Science Research (BINDS)) to S.P.

Conflict of Interest

The authors declare no conflict of interest.

Data Availability Statement

The data that support the findings of this study are available from the corresponding author upon reasonable request.

Keywords

arylazopyrazole photo-switches, DNA structures, drug delivery, NIR-controlled drug release, upconversion nanoparticles

Received: October 15, 2024
Revised: January 20, 2025
Published online: February 25, 2025

[1] Y. Sasai, *Nature* **2013**, *493*, 318.
[2] A. P. McGuigan, S. Javaherian, *Annu. Rev. Biomed. Eng.* **2016**, *18*, 1.
[3] M. A. Kinney, T. C. McDevitt, *Trends Biotechnol.* **2013**, *31*, 78.
[4] F. Guillemot, *Development* **2007**, *134*, 377180.
[5] M. Kohwi, C. Q. Doe, *Nat. Rev. Neurosci.* **2013**, *14*, 823.
[6] R. S. Liu, L. U. Colmenares, *Proc. Natl. Acad. Sci. USA* **2003**, *100*, 14639.
[7] A. H. Gelebart, D. Jan Mulder, M. Varga, A. Konya, G. Vantomme, E. W. Meijer, R. L. B. Selinger, D. J. Broer, *Nature* **2017**, *546*, 632.
[8] M. M. Lerch, M. J. Hansen, G. M. van Dam, W. Szymanski, B. L. Feringa, *Angew Chem Int Ed Engl* **2016**, *55*, 10978.
[9] H. M. Bandara, S. C. Burdette, *Chem. Soc. Rev.* **2012**, *41*, 1809.
[10] V. Adam, D. K. Prusty, M. Centola, M. Skugor, J. S. Hannam, J. Valero, B. Klockner, M. Famulok, *Chemistry* **2018**, *24*, 1062.
[11] Y. Kamiya, H. Asanuma, *Acc. Chem. Res.* **2014**, *47*, 1663.
[12] D. Y. Tam, X. Zhuang, S. W. Wong, P. K. Lo, *Small* **2019**, *15*, e1805481.
[13] M. Zhu, H. Zhou, *Org. Biomol. Chem.* **2018**, *16*, 8434.
[14] A. A. Beharry, O. Sadovski, G. A. Woolley, *J. Am. Chem. Soc.* **2011**, *133*, 19684.
[15] S. Mishra, S. Park, T. Emura, H. Kumi, H. Sugiyama, M. Endo, *Chemistry* **2021**, *27*, 778.
[16] C. E. Weston, R. D. Richardson, P. R. Haycock, A. J. White, M. J. Fuchter, *J. Am. Chem. Soc.* **2014**, *136*, 11878.
[17] L. Stricker, E. C. Fritz, M. Peterlechner, N. L. Doltsinis, B. J. Ravoo, *J. Am. Chem. Soc.* **2016**, *138*, 4547.
[18] C. Ash, M. Dubec, K. Donne, T. Bashford, *Lasers Med. Sci.* **2017**, *32*, 1909.
[19] X. Wu, G. Chen, J. Shen, Z. Li, Y. Zhang, G. Han, *Bioconjug. Chem.* **2015**, *26*, 166.
[20] C. Wang, X. Li, F. Zhang, *Analyst* **2016**, *141*, 3601.
[21] M. K. Mahata, R. De, K. T. Lee, *Biomedicines* **2021**, *9*, 756.
[22] M. F. Torresan, A. Wolosiuk, *ACS Appl. Bio Mater.* **2021**, *4*, 1191.
[23] P. Jethva, M. Momin, T. Khan, A. Omri, *Materials* **2022**, *15*, 2374.
[24] G. Chen, H. Qiu, P. N. Prasad, X. Chen, *Chem. Rev.* **2014**, *114*, 5161.
[25] H. Li, X. Wang, T. Y. Ohulchanskyy, G. Chen, *Adv. Mater.* **2021**, *33*, 2000678.
[26] H. Chen, B. Ding, P. Ma, J. Lin, *Adv. Drug Deliv. Rev.* **2022**, *188*, 114414.
[27] D. Li, S. Wen, M. Kong, Y. Liu, W. Hu, B. Shi, X. Shi, D. Jin, *Anal. Chem.* **2020**, *92*, 10913.
[28] K. Malhotra, D. Hrovat, B. Kumar, G. Qu, J. V. Houten, R. Ahmed, P. A. E. Piunno, P. T. Gunning, U. J. Krull, *ACS Appl. Mater. Interfaces* **2023**, *15*, 2499.
[29] Y. Zhang, L. M. Wiesholler, H. Rabie, P. Jiang, J. Lai, T. Hirsch, K. B. Lee, *ACS Appl. Mater. Interfaces* **2020**, *12*, 40031.
[30] H. Rabie, Y. Zhang, N. Pasquale, M. J. Lagos, P. E. Batson, K. B. Lee, *Adv. Mater.* **2019**, *31*, 1806991.
[31] X. Yang, D. Song, L. Chen, H. Xiao, X. Ma, Q. Jiang, O. Cheng, *Brain Res.* **2021**, *1751*, 147197.
[32] S. K. Tiwari, S. Agarwal, B. Seth, A. Yadav, S. Nair, P. Bhatnagar, M. Karmakar, M. Kumari, L. K. Chauhan, D. K. Patel, V. Srivastava, D. Singh, S. K. Gupta, A. Tripathi, R. K. Chaturvedi, K. C. Gupta, *ACS Nano* **2014**, *8*, 76.
[33] C. Wang, X. Zhang, Z. Teng, T. Zhang, Y. Li, *Eur. J. Pharmacol.* **2014**, *740*, 312.
[34] J. H. Kim, S. H. Park, S. W. Nam, H. J. Kwon, B. W. Kim, W. J. Kim, Y. H. Choi, *Int. J. Mol. Med.* **2011**, *28*, 429.
[35] C. Buhrmann, A. Mobasheri, U. Matis, M. Shakibaei, *Arthritis Res. Ther.* **2010**, *12*, R127.
[36] S. J. Kim, T. G. Son, H. R. Park, M. Park, M. S. Kim, H. S. Kim, H. Y. Chung, M. P. Mattson, J. Lee, *J. Biol. Chem.* **2008**, *283*, 14497.
[37] S. K. Tiwari, S. Agarwal, A. Tripathi, R. K. Chaturvedi, *Mol. Neurobiol.* **2016**, *53*, 3010.
[38] F. Aleotti, A. Nenov, L. Salvigni, M. Bonfanti, M. M. El-Tahawy, A. Giunchi, M. Gentile, C. Spallacci, A. Ventimiglia, G. Cirillo, L. Montali, S. Scurti, M. Garavelli, I. Conti, *J. Phys. Chem. A* **2020**, *124*, 9513.
[39] W. A. Wee, H. Sugiyama, S. Park, *iScience* **2021**, *24*, 103455.
[40] T. Hidaka, W. A. Wee, J. H. Yum, H. Sugiyama, S. Park, *Bioconjug. Chem.* **2021**, *32*, 2129.
[41] J. H. Yum, T. Ishizuka, K. Fukumoto, D. Hori, H. L. Bao, Y. Xu, H. Sugiyama, S. Park, *ACS Biomater. Sci. Eng.* **2021**, *7*, 1338.
[42] J. H. Yum, T. Kumagai, D. Hori, H. Sugiyama, S. Park, *Nanoscale* **2023**, *15*, 10749.
[43] J. H. Yum, H. Sugiyama, S. Park, *Chem. Rec.* **2022**, *22*, 202100333.
[44] E. M. Chan, E. S. Levy, B. E. Cohen, *Adv. Mater.* **2015**, *27*, 5753.
[45] B. Zhou, B. Tang, C. Zhang, C. Qin, Z. Gu, Y. Ma, T. Zhai, J. Yao, *Nat. Commun.* **2020**, *11*, 1174.
[46] A. B. Kostyuk, A. D. Vorotnov, A. V. Ivanov, A. B. Volovetskiy, A. V. Kruglov, L. M. Sencha, L. Liang, E. L. Guryev, V. A. Vodeneev, S. M. Deyev, Y. Lu, A. V. Zvyagin, *Nano Res.* **2019**, *12*, 2933.
[47] M.-F. Joubert, *Opt. Mater.* **1999**, *11*, 181.
[48] A. Skripka, M. Lee, X. Qi, J.-A. Pan, H. Yang, C. Lee, P. J. Schuck, B. E. Cohen, D. Jaque, E. M. Chan, *Nano Lett.* **2023**, *23*, 7100.
[49] E. Koren, A. Apte, R. R. Sawant, J. Grunwald, V. P. Torchilin, *Drug Deliv.* **2011**, *18*, 377.
[50] S. Ghosh, S. Mallick, U. Das, A. Verma, U. Pal, S. Chatterjee, A. Nandy, K. D. Saha, N. C. Maiti, B. Baishya, G. Suresh Kumar, W. H. Gmeiner, *Biochim. Biophys. Acta Gen. Subj.* **2018**, *1862*, 485.
[51] F. Zsila, Z. Bikadi, M. Simonyi, *Org. Biomol. Chem.* **2004**, *2*, 2902.
[52] J. Chen, Z. M. He, F. L. Wang, Z. S. Zhang, X. Z. Liu, D. D. Zhai, W. D. Chen, *Eur. J. Pharmacol.* **2016**, *772*, 33.
[53] S. J. Hewlings, D. S. Kalman, *Foods* **2017**, *6*, 92.
[54] M. Ashrafizadeh, Z. Ahmadi, R. Mohamamdinejad, H. Yaribeygi, M. C. Serban, H. M. Orafai, A. Sahebkar, *Curr. Pharm. Biotechnol.* **2020**, *21*, 1006.
[55] M. Wang, Z. Xu, Q. Liu, W. Sun, B. Jiang, K. Yang, J. Li, Y. Gong, Q. Liu, D. Liu, X. Li, *Biomaterials* **2019**, *225*, 119539.